Soft Matter

Lipid Anchor Display on Peptoid Nanosheets *via* Co-Assembly for Multivalent Pathogen Recognition

SCHOLARONE™
Manuscripts

Lipid Anchor Display on Peptoid Nanosheets *via* Co-Assembly for Multivalent Pathogen Recognition

Jae Hong Kim,[a] Elissa M. Grzincic,[a] Lisa Yun,[a] Ryan K. Spencer,[b] Mark A. Kline[a] and Ronald N. Zuckermann[*a]

Biological systems have evolved sophisticated molecular assemblies capable of exquisite molecular recognition across length scales ranging from angstroms to microns. For instance, the self-organization of glycolipids and glycoproteins on cell membranes allows for molecular recognition of an incredible diversity of ligands ranging from small molecules and proteins to viruses and whole cells. A distinguishing feature of these 2D surfaces is they achieve exceptional binding selectivity and avidity by exploiting multivalent binding interactions. Here we develop a 2D ligand display platform based on peptoid nanosheets that mimics the structure and function of the cell membrane. A variety of small-molecule lipid-conjugates were co-assembled with the peptoid chains to create a diversity of functionalized nanosheet bilayers with varying display densities. The functional heads of the lipids were shown to be surface-exposed, and the carbon tails immobilized into the hydrophobic interior. We demonstrate that saccharide-functionalized nanosheets (e.g., made from globotriaosylsphingosine or 1,2-dipalmitoyl-sn-glycero-3-phospho((ethyl-1',2',3'-triazole)triethyleneglycolmannose) can have very diverse binding properties, exhibiting specific binding to multivalent proteins as well as to intact bacterial cells. Analysis of sugar display densities revealed that Shiga toxin 1 subunit B (a pentameric protein) and FimH-expressing *Escherichia coli* (*E. coli*) bind through the cooperative binding behavior of multiple carbohydrates. The ability to readily incorporate and display a wide variety of lipidated cargo on the surface of peptoid nanosheets makes this a convenient route to soluble, cell-surface mimetic materials. These materials hold great promise for drug screening, biosensing, bioremediation, and as a means to combat pathogens by direct physical binding through a well-defined, multivalent 2D material.

Introduction

Peptoids are bio-inspired sequence-defined *N*-substituted glycine polymers that can be efficiently and cost-effectively synthesized from a variety of amine monomers to achieve stability and side chain diversity superior to natural peptides.[1,2] Depending on the monomer sequence, peptoids can fold into various protein-like architectures such as helices, ribbons, loops, cyclic structures, multi-helical bundles, superhelices, and nanosheets.[3-6] One particularly promising platform is based on free-floating, surface-functionalized peptoid nanosheets. Our lab and others have reported antibody-mimetic peptoid nanosheets constructed by the self-assembly of amphiphilic peptoids containing an inserted loop-forming domain in the middle of sequence.[7-9] The surface of nanosheets was decorated by loops that could recognize specific protein targets depending on the loop sequence. These nanosheets exhibit superior chemical and biological stability, and the ability to recognize ligands *via* multivalent interactions.

2D biocompatible nanomaterials that can be readily functionalized are gaining attention as mimetics of cellular membranes. The cell membrane consists of 5 nm phospholipid bilayers with embedded functional molecules, often highly glycosylated, that are essential for molecular recognition, cellular signaling, molecular transport, and energy conversion (**Figure 1a**).[10] The synchronous binding of numerous carbohydrates to a number of receptors enables exquisite molecular recognition with high sensitivity and selectivity. In nature, pathogens (e.g., virus, bacteria, and fungi) maneuver this phenomenon for efficient adhesion to the glycocalyx to initiate infection. Diverse multivalent 0- and 1-dimensional scaffolds have been designed to mimic some cell surface features, in order to efficiently detect pathogens and as a means to inhibit infectivity.[11-18] However, the receptor binding ligands of these types of scaffolds can be concealed by the formation of sterically shielding domains. In this regard, 2-dimensional nanomaterials have a high potential for multivalent display scaffolds.[19]

We previously developed two synthetic routes to create functionalized peptoid nanosheets,[9] either by: (1) first incorporating the display element into the peptoid sequence, and then assembling it into a nanosheet, or (2) forming the nanosheet first, and then conjugating a display element to the sheet surface. The former is generally preferred, since

[a.] Molecular Foundry, Lawrence Berkeley National Laboratory, 1 Cyclotron Road, Berkeley California 94720, USA
[b.] Department of Chemistry and Department of Chemical Engineering & Materials Science, University of California, Irvine, Irvine, California, USA
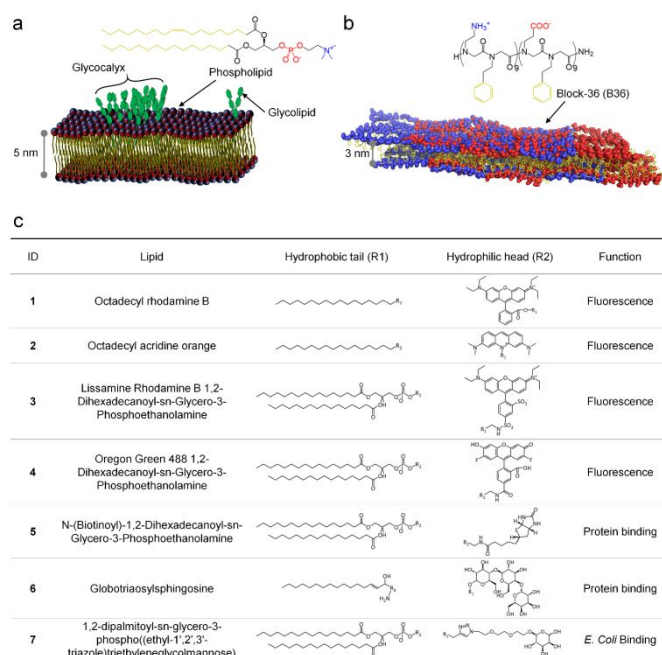
ARTICLE

Soft Matter

Figure 1. Structural similarity of peptoid nanosheets to a cell membrane. (a) Schematic illustration of cell membrane composed of phospholipids and glycolipids. Glycolipids dynamically self-organized into glycocalyx on the surface of cell membrane. (b) Molecular model of a peptoid nanosheet.[25] Block-patterned peptoid strands (B36) folded into brick-like patterned bilayer nanosheets similar to the phospholipid bilayer. (c) Chemical structure of various lipids as fluorophores and protein/*E. coli* binders for the functionalization of peptoid nanosheets.

nanosheet assembly can occur with a purified peptoid leading directly to the desired product. The latter approach has the advantage of creating a common nanosheet intermediate to which a variety of ligands can be attached, but also requires a post-conjugation nanosheet purification step. Because these biomimetic materials hold great promise for a variety of biomedical applications, we sought an even more efficient method to create this class of functionalized 2D nanomaterial. In the present work, we combine the advantages of both these approaches by a non-covalent co-assembly approach, where a nanosheet-forming peptoid is first combined with a lipid-conjugated small molecule, and then assembled into a nanosheet. This step-wise assembly process is made possible by the fact that peptoid nanosheet assembly does not occur until triggered by the lateral compression of a peptoid monolayer at the air-water interface.[20-24]

Peptoid nanosheets were built from the self-assembly of amphiphilic peptoid strands consisting of the patterned sequence of alternating hydrophobic and charged monomers (**Figure 1b**). The zwitterionic and flat surface of peptoid nanosheets are well-suited for 2D multivalent scaffolds because sterically shielding domains and non-specific interferent binding are prevented. Moreover, the hydrophobic aromatic core of the nanosheet (about 2 nm thick) allows for the penetration of small hydrophobic molecules, and thus provides a new opportunity to anchor lipidated molecules with polar functional head groups.[25, 26] We demonstrated this route to the functionalization of peptoid nanosheets by co-assembly with assorted lipids containing diverse functional hydrophilic
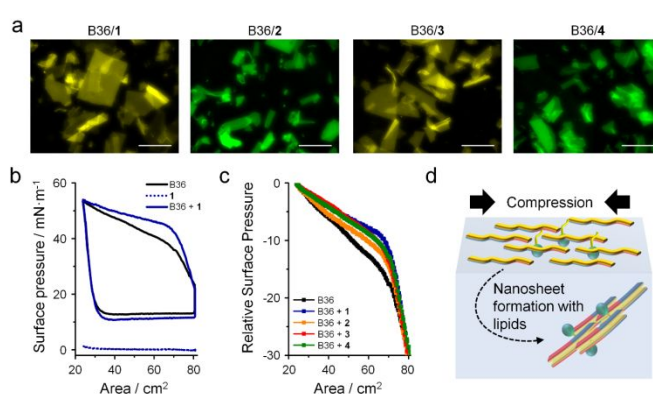

Figure 2. Self-assembly of peptoid strands with lipids. (a) Fluorescent microscopic images of co-assemblies B36/**1**, **2**, **3** and **4**. The images of B36/**1** and **3** were taken under a yellow (Texas Red) filter. The images of B36/**2** and **4** were taken under a green (fluorescein) filter. All scale bars represent 10 μm. (b) Langmuir isotherms of 20 μM B36 (black solid line), 10 μM **1** (blue dotted line) and 20 μM B36 with 10 μM **1** (blue solid line). The curves were obtained at a compression/expansion rate of 100 cm^2 min^{-1} with a wait time of 450 s between compression and expansion. (c) 100 cm^2 min^{-1} Compression isotherms of 20 μM B36 without (black) and with 10 μM **1** (blue), **2** (orange), **3** (green), and **4** (red). Isotherms are normalized to the surface pressure of collapse. (d) Suggested formation mechanism of peptoid nanosheets with lipids at the air-water interface. Peptoid strands mostly occupy the interface while lipids exist in empty surface spaces. When lateral compression is applied, lipids are assembled into peptoid nanosheets.

head groups (**Figure 1c**). Structural analyses (XRD, AFM and MD simulation) showed that the hydrophilic heads of lipids were located onto the surface of peptoid nanosheets, while the hydrophobic tails of lipids were favored to immobilize into the hydrophobic interior of peptoid nanosheets. In this manner, globotriaosylated sheets could be readily made which exhibit sensitive and selective binding for Shiga toxin 1 subunit B (a pentameric protein), as well as mannosylated sheets which efficiently bind to *E. coli* as a model pathogen.

Results & Discussion

First, we examined the self-assembly of block-36 strands (B36) with dye-conjugated lipids (**1** − **4**) to visually observe the co-assembly of lipids into peptoid nanosheets by fluorescence microscopy. We previously showed that surfactants, such as Zwittergent 3-12 (n-dodecyl-*N,N*-dimethyl-3-ammonio-1-propanesulfonate), at concentrations above 30 μM disrupt peptoid monolayer formation at the air-water interface[27]. To avoid this potentially inhibiting effect, we kept the dye-conjugated lipid concentration below a concentration of 10 μM. After initiating self-assembly by repetitive surface compression and expansion (*via* the vial rocking method),[24] we found that the fluorescence of **1** − **4** appeared in regions corresponding with nanosheets (**Figure 2a**). We denote these co-assemblies as "B36/**x**" where **x** represents the lipid component molecule. On the contrary, indistinct fluorescence with high background was observed when B36 strands were co-assembled with non-

lipidated fluorophores, or with the fluorescent lipid alone (**Figure S1**). These results indicate that the lipid tails are crucial components for their incorporation into peptoid nanosheets. To convincingly understand the formation mechanism, we explored Langmuir trough isotherms of peptoid B36 strands in the presence of 10 μM **1** − **4** (**Figure 2b and S2**). Consistent with the sheet production cycle of B36 strands at the air-water interface,[24] isotherms of B36 strands with **1** − **4** exhibited the expected four distinct regions of: adsorption, compression, collapse, and expansion. The isotherms of **1** − **4** alone showed gas-like behavior of lipids on the interface,[28] suggesting lipids can incorporate into the peptoid monolayer and bilayer when peptoid strands are self-assembled at the air-water interface. We also confirmed nanosheet formation in the presence of **1** − **4** by quantitating the relative yield of peptoid nanosheets by optical microscopy (**Figure S3**).[27] Another interesting observation from the Langmuir isotherms of nanosheet formation was that the presence of lipids actually increased the collapse pressure (**Figure 2c**). As the surface pressure is proportional to the number of molecules at the air-water interface,[29] we envision that peptoid strands and lipids favorably interact on the surface and are able to collapse into bilayers with a higher density of molecules as compared with the assembly of *only* peptoid strands (**Figure 2d**). This favorable interaction likely translates to stable anchoring of the lipid within the peptoid nanosheets, unlike in lipid bilayers, which spontaneously disassemble and reform in an aqueous solution. We monitored the stability of the lipid co-assemblies to desorption by examining their fluorescence after dialysis in buffer. The initial fluorescence intensity of B36/**1** − B36/**4** reduced by <5% after overnight dialysis against water (**Figure S4**), meaning that lipids were firmly immobilized in peptoid nanosheets. Taken together, we established a simple, modular and efficient functionalization strategy for peptoid nanosheets *via* the co-assembly of peptoid strands with lipids at the air-water interface.

Based on the formation mechanism of peptoid/lipid hybrid nanosheets, the hydrophilic heads of the lipids are expected to be exposed to water on the surface of the nanosheets. In order to study the solvent accessibility of the hydrophilic heads, we examined the Stern-Volmer relationship between **1**-incorporated peptoid nanosheets (B36/**1**) and potassium iodide (KI), which is a conventional collisional fluorescence quencher to examine the location of tryptophan and dye in proteins and bilayer membranes.[30] As controls, we also employed Alexa Fluor 488-conjugated peptoid nanosheets (Alexa488-B36), and Nile Red-incorporated peptoid nanosheets (B36/NR). Note that the fluorescence of Alexa Fluor 488 should quench in the presence of KI because Alexa Fluor 488 was conjugated onto the charged side chain of B36 strands. However, KI should not affect the fluorescence of B36/NR because NR, which only fluoresces in hydrophobic environments, is embedded in the phenyl-rich domain of the nanosheets concealed in the center of the bilayer. As expected, the fluorescence intensity of Alexa488-B36 significantly diminished with the increase of the concentration of KI in contrast with NR/B36 (**Figure 3a**). We found that the
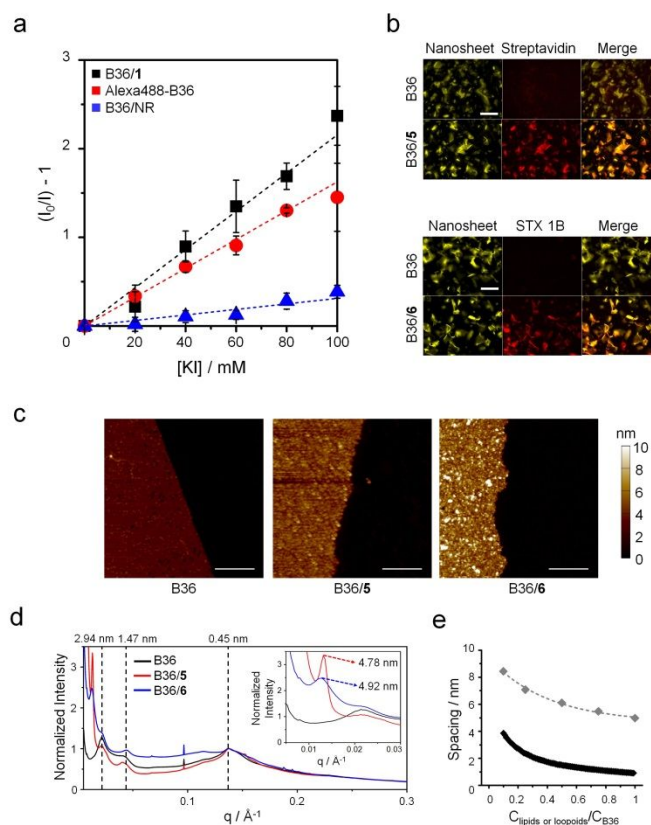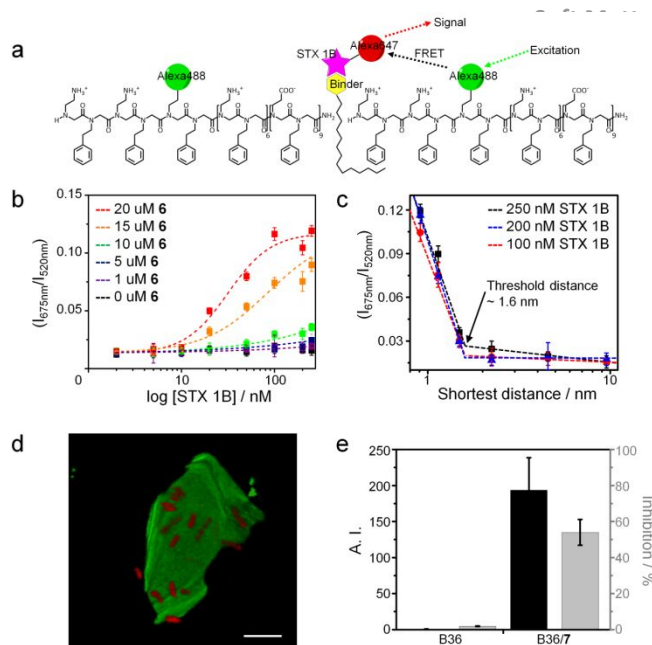

Figure 3. Study of the molecular structure of lipids-incorporated peptoid nanosheets. (a) Stern-Volmer plot of B36/**1**, B36/NR and Alexa488-B36 as a function of KI concentration. (b) Fluorescent microscope images of B36, B36/**5**, and B36/**6** in the absence and presence of Alexa647-conjugated streptavidin and STX 1B. Yellow (Texas Red) and far-red (Cy5) filters were used for imaging of NR-staining peptoid nanosheets and Alexa647-conjugated proteins, respectively. All scale bars represent 100 μm. (c) AFM images (scale bars represent 1 μm) and (d) XRD spectra of B36, B36/**5**, and B36/**6**. Inset shows the increased thickness of lipid-incorporated peptoid nanosheets. (e) Relationship between spacing and density of lipids (gray) or loops (black). The lipid spacing is based on the average distance between lipids estimated by FRET analysis using B36/(**1** and **2**) (**Figure S5**). The loop spacing is based on the simulation of shortest distance between loops against the fraction of loops.

fluorescence of B36/**1** dramatically quenched with the addition of KI, similar to Alexa488-B36. We quantitatively compared the Stern-Volmer constant (K_{SV}) of B36/**1**, B36/Alexa488, B36/NR, and free NR in DMF. The K_{SV} of B36/**1** (~ 24 M^{-1}) is in the range of the K_{SV} of Alexa488-B36 (~ 16.5 M^{-1}) and free Nile Red in DMF (19.5 M^{-1})[31], but is 8 times higher than the K_{SV} of B36/NR (~ 3.3 M^{-1}). This indicates that the hydrophilic heads of **1** are exposed on the surface of peptoid nanosheets and have similar degrees of freedom as free molecules in solution. This suggests this display method is suitable for binding to proteins and other biomacromolecules. We prepared peptoid nanosheets co-assembled with **5** and **6** (B36/**5** and B36/**6**), containing biotin and globotriose which are known ligands for streptavidin and Shiga toxin 1 subunit B (STX 1B), respectively. Fluorescence microscopy reveals that the fluorescence of Alexa Fluor 647-

ARTICLE

conjugated streptavidin and STX 1B under a far-red Cy5 filter was exactly colocalized with that of B36/**5** and /**6** stained by Nile Red under a yellow Texas Red filter (**Figure 3b**). Conversely, un-functionalized peptoid nanosheets do not show red emission. These observations clearly show that the hydrophilic heads of lipids were displayed onto the surface of peptoid nanosheets and can readily bind to their cognate proteins.

We further investigated the molecular structure of lipid-incorporated peptoid nanosheets using atomic-force microscopy (AFM) and x-ray diffraction (XRD) analysis. AFM images show that the thickness of peptoid nanosheets (~ 2.9 nm) increased upon co-assembly with **5** (~ 4.7 nm) and **6** (~ 5.0 nm) (**Figure 3c**). Nanosheet thickness has been shown to correlate somewhat with steric accessibility of the functional groups. For example, Battigelli *et al.* found that coupling monosaccharides to a nanosheet with a very short linker resulted in no change in sheet thickness, and a loss of lectin binding activity.[9] However, the binding activity was recovered when the sugars were displayed on loops that protrude out from the surface. The thickness scale of B36/**5** and /**6** are comparable to that of the 8mer loop-functionalized peptoid.[8] Thus, the AFM measurement supported that there is sufficient protrusion of the functional heads to enable protein binding. The powder XRD patterns of B36/**5** and /**6** showed that they possess an ordered structure similar to previously reported nanosheet XRD.[25, 32] Specifically, the diffraction pattern showed a characteristic peak at 4.6 Å, attributed to the spacing between peptoid strands, as well as a 2.8 nm peak originating from the thickness of the peptoid bilayer (**Figure 3d**). The lipid-loaded nanosheets also exhibited increased thickness by XRD, correlating with the AFM data. It seems that the lipid incorporation did not interfere with the inherent molecular structure of the peptoid nanosheets. We posit that pockets which are thought to exist between the termini of peptoid strands are possible sites for the immobilization of lipids into peptoid nanosheets without the interruption because small molecules, such as water, can penetrate the pockets without structure deformation of peptoid nanosheets under molecular dynamic (MD) simulations.[33] These pockets extend into the hydrophobic nanosheet interior, providing a site with exposed aromatic residues that likely interact with the lipid tail. According to the molecular structure of peptoid nanosheets,[25] the average distance between pockets is 5.1 nm, which is close to the distance between lipid at 4.9 nm as estimated by FRET analysis (**Figure S5**), consistent with most lipids incorporating into the pockets. We further quantified the lipid spacing by varying their concentration (and therefore the display density) for a comparison with loop-functionalized peptoid nanosheets (**Figure 3e**). They should have common features because the arrangement of loops is identical with the pockets of peptoid nanosheets (**Figure S6**). For this comparison, we adopted the calculation of shortest loop distance against loop density according to a previous report.[9] Although the spacing of lipids and loops were not of similar values due to different mathematical approaches (shortest distance for loops vs. average distance for lipids), the spacing increased exponentially with decreasing density in both cases, suggesting that the lipids

were immobilized in the pockets of peptoid nanosheets. Indeed, the molecular structure of B36/**5** and B36/**6** by MD simulations showed that carbon tails were stable in the pockets while they escaped from spacing between peptoid strands (**Figure S7**).

Figure 4. Protein and bacteria binding to lipid-incorporated peptoid nanosheets. (a) Schematic illustration of a homogeneous FRET assay for the validation of protein binding to peptoid nanosheets (b) FRET ratio of peptoid nanosheets with varying concentrations of **6** as a function of the concentration of STX 1B. (c) FRET ratio of B36/**6** as a function of the shortest distance between lipids on the nanosheets. (d) Confocal images of B36/**7** in the presence of *E. coli* ORN178. Green is peptoid nanosheets due to Alexa488 conjugation to B36 strands. Red is *E. coli* stained by red fluorescent protein. Scale bar represent 5 μm (e) Agglutination index (A.I.) (black) and growth inhibition (gray) of *E. coli* ORN178 in the presence of B36 and B36/20 μM **7**. *E. coli* were grown in LB medium and the degree of growth inhibition was measured after 5 hr.

In order to use these constructs to mimic the glycocalyx on the cell membrane, we investigated the binding response of B36/**6** against STX 1B, a protein homopentamer, which contains binding sites for globotriose in each subunit (**Figure S8**). We employed a homogeneous FRET assay using Alexa Fluor 488-conjugated peptoid strands (i.e., FRET donors) and Alexa Fluor 647-conjugated STX 1B (i.e., FRET acceptors) to determine protein binding on the surface of peptoid nanosheets, (**Figure 4a**). The farthest distance (~ 1.8 nm) from Alexa Fluor 647 of STX 1B to the Alexa Fluor 488 of the fifth position of B36 strands is enough for FRET because the FRET radius of Alexa Fluor 488/Alexa Fluor 647 is 5.6 nm.[34] As expected, the FRET signal at 675 nm appeared with the concurrent decrease of Alexa Fluor 488 emission at 520 nm in B36/**6** samples in the presence of 250 nM STX 1B, whereas the spectrum of un-functionalized peptoid nanosheets is maintained (**Figure S9**). In previous studies, it was shown that peptoid nanosheets containing numerous

functional binding ligands on their surface have the ability to make multivalent binding interactions to target proteins.[8,9] The density of surface-displayed lipids can be controlled by varying the lipid component concentration during the assembly, which is ideal to observe the multivalency of lipid-displayed peptoid nanosheets. We analyzed the plot of FRET ratio ($I_{675\,nm}/I_{520\,nm}$) against the concentration of STX 1B interacting with B36 nanosheets with a range of concentrations of **6** incorporated (**Figure 4b**). In nanosheets with **6** above 15 μM, the binding curve was non-linear; the FRET ratio was rapidly increased and saturated within the narrow concentration range of STX 1B from 10 to 100 nM. The non-linear response can be explained by previous reports,[35, 36] where multivalency provides super-selectivity characterized by the steep change of binding degree within a narrow concentration range. Assuming that the average shortest distance between lipids is identical with that between loops as described above, we plotted FRET ratio versus the average shortest distance between **6** varying with the concentration of STX 1B (**Figure 4c**). We observed a dramatic increase in STX 1B binding when **6** are less than 1.6 nm apart from each other. The threshold distance is well in line with the shortest distance between binding sites on STX 1B (~1.4 nm) (**Figure S8**). This indicates that the arrangement of lipids on peptoid nanosheets enables cooperative binding behavior over multiple carbohydrates. We further quantified the apparent dissociation binding constant (K_D) using the fitting of binding curve by Hill's equation.[37] K_D of peptoid nanosheets hybridized with 20 μM **6** for STX 1B was approximately 32×10^{-9} M. Without the assistance of the peptoid scaffolds, the K_D of univalent globotriose for STX 1B is $1 \sim 2 \times 10^{-3}$ M.[38] Taken together, peptoid/lipid hybrid nanosheets can serve as multivalent scaffolds to capture target proteins with high selectivity and sensitivity.

These biologically active, lipid-anchor display nanosheets are in fact microns in lateral dimension, which opens up exciting possibilities to use them for molecular recognition of much larger bioassemblies, like intact virus particles and microbial cells. Indeed, bio-specific 2D nanomaterials are recognized to have great potential to combat pathogens.[39] In order to ascertain the ability of lipid-anchored peptoid nanosheets to specifically recognize and bind to an entire living cell, we prepared nanosheets incorporating a DMPE-linked mannose derivative (B36/**7**) and bound them under physiological conditions to *E. coli* as a model pathogen. In particular, we introduced *E. coli* ORN178, a K-12 derivative strain that expresses mannose-specific adhesin FimH of type 1 pili on its surface to interact with mannose of **7**.[40, 41] We also used *E. coli* ORN208, which lacks the FimH receptor, as a negative control.[41] Confocal microscopy shows that 20 μM the B36/**7** nanosheets captured *E. coli* ORN178 on their surface, whereas B36 had no binding activity for *E. coli* ORN178 (**Figure 4d** and **S10**). In another negative control, we observed no binding of *E. coli* ORN208 to B36/**7**. Additionally, B36/**7**'s binding affinity disappeared when the concentration of **7** was lowered to 10 μM (**Figure S11**), indicating that a high display density of **7** facilitated the efficient and selective binding affinity for *E. coli* ORN178 *via* multivalent interactions. Binding of *E. coli* to the B36/7 was rapid and efficient, with multiple individual bacteria binding to a single sheet. This suggests that these materials may find utility in detecting or neutralizing microbes.

We further found that quite a number of *E. coli* ORN178 were settled on the surface of **7**-incorporated peptoid nanosheets compared to un-functionalized nanosheets using fluorescent microscopy (**Figure S12**). This observation gives a hint to use the lipid-displayed peptoid nanosheets to prevent the growth of pathogens because the aggregation and encirclement of *E. coli* by multivalent scaffolds is known to inhibit their proliferation.[42, 43] We first quantified the capturing ability of one lipids-incorporated peptoid nanosheet for *E. coli* by agglutination index (A.I.) according to the literature.[42, 44] The A.I. value of B36/**7** at approximately 198 was comparable with mannose-functionalized peptide nanotubes and graphene.[43, 45] To explore whether the physical binding of the B36/**7** sheets to *E. coli* would interfere with their proliferation, we measured the growth of *E. coli* ORN178 in the presence of B36 and B36/**7** sheets. The inhibition of bacterial growth by B36/**7** was approximately 50% while B36 had no effect (**Figure 4e**). Without the arrangement of mannose by peptoid scaffolds, peptoid scaffolds *itself* or free mannose derivatives only slightly trigger to *E. coli* aggregation and their growth inhibition. Thus, the lipid-anchored peptoid nanosheets appear ideally suited as candidate materials to neutralize pathogens by direct binding.

Conclusions

In conclusion, we successfully demonstrated the modular functionalization of peptoid nanosheets by their co-assembly with various lipids to create a class of tunable 2D nanomaterials that can mimic the structure and aspects of the function of the cell membrane. We demonstrate that our lipid anchoring strategy results in stable constructs that are competent for protein binding under physiological conditions. The display density of the anchored ligands can be tuned, enabling the recognition of targets with high selectivity and sensitivity via multivalent interactions. The micron-scale dimensions of the sheets allows them to be used to directly bind bacterial cells and inhibition their growth, opening the door to new mechanisms to combat pathogens. Therefore, the co-assembly of peptoids with lipids opens an efficient new route to create stable, biocompatible, 2-dimensional multivalent scaffolds with tunable structures, enabling new opportunities in biomedicine.

Conflicts of interest
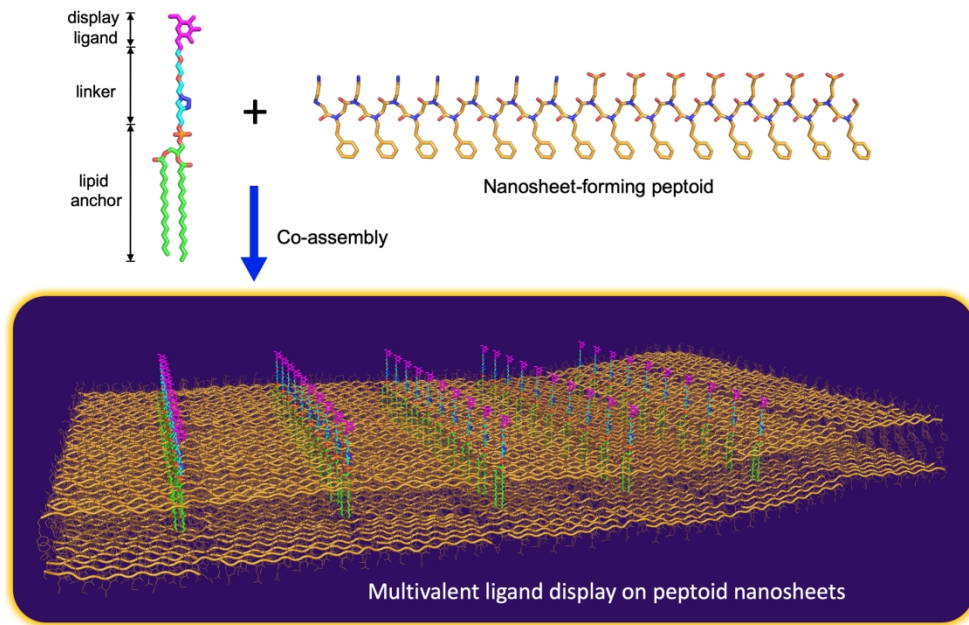
There are no conflicts to declare.

Acknowledgements

ARTICLE **Soft Matter**

Science, Office of Basic Energy Sciences, U.S. Department of Energy under contract no. DEAC02-05CH11231.

Notes and references

1   A. S. Knight, E. Y. Zhou, M. B. Francis and R. N. Zuckermann, *Adv. Mater.*, 2015, **27**, 5665-5691.
2   J. Sun and R. N. Zuckermann, *ACS Nano*, 2013, **7**, 4715-4732.
3   J. A. Crapster, I. A. Guzei and H. E. Blackwell, *Angew. Chem. Int. Ed.*, 2013, **52**, 5079-5084.
4   H. K. Murnen, A. M. Rosales, J. N. Jaworski, R. A. Segalman and R. N. Zuckermann, *J. Am. Chem. Soc.*, 2010, **132**, 16112-16119.
5   S. B. Shin, B. Yoo, L. J. Todaro and K. Kirshenbaum, *J. Am. Chem. Soc.*, 2007, **129**, 3218-3225.
6   C. W. Wu, T. J. Sanborn, K. Huang, R. N. Zuckermann and A. E. Barron, *J. Am. Chem. Soc.*, 2001, **123**, 6778-6784.
7   L. Zhu, Z. Zhao, P. Cheng, Z. He, Z. Cheng, J. Peng, H. Wang, C. Wang, Y. Yang and Z. Hu, *Adv. Mater.*, 2017, **29**.
8   G. K. Olivier, A. Cho, B. Sanii, M. D. Connolly, H. Tran and R. N. Zuckermann, *ACS Nano*, 2013, **7**, 9276-9286.
9   A. Battigelli, J. H. Kim, D. C. Dehigaspitiya, C. Proulx, E. J. Robertson, D. J. Murray, B. Rad, K. Kirshenbaum and R. N. Zuckermann, *ACS Nano*, 2018, **12**, 2455-2465.
10 D. Lingwood and K. Simons, *Science*, 2010, **327**, 46-50.
11 T. D. Farr, C.-H. Lai, D. Grünstein, G. Orts-Gil, C.-C. Wang, P. Boehm-Sturm, P. H. Seeberger and C. Harms, *Nano Lett.*, 2014, **14**, 2130-2134.
12 G. Yu, J. Li, W. Yu, C. Han, Z. Mao, C. Gao and F. Huang, *Adv. Mater.*, 2013, **25**, 6373-6379.
13 Y. Chen, H. Vedala, G. P. Kotchey, A. Audfray, S. Cecioni, A. Imberty, S. Vidal and A. Star, *ACS Nano*, 2012, **6**, 760-770.
14 C.-H. Lai, C.-Y. Lin, H.-T. Wu, H.-S. Chan, Y.-J. Chuang, C.-T. Chen and C.-C. Lin, *Adv. Funct. Mater.*, 2010, **20**, 3948-3958.
15 P. Compain, C. Decroocq, J. Iehl, M. Holler, D. Hazelard, T. Mena Barragán, C. Ortiz Mellet and J.-F. Nierengarten, *Angew. Chem. Int. Ed.*, 2010, **49**, 5753-5756.
16 I. van Baal, H. Malda, S. A. Synowsky, J. L. J. van Dongen, T. M. Hackeng, M. Merkx and E. W. Meijer, *Angew. Chem. Int. Ed.*,, 2005, **44**, 5052-5057.
17 P. M. Rendle, A. Seger, J. Rodrigues, N. J. Oldham, R. R. Bott, J. B. Jones, M. M. Cowan and B. G. Davis, *J. Am. Chem. Soc.*, 2004, **126**, 4750-4751.
18 C.-C. Lin, Y.-C. Yeh, C.-Y. Yang, C.-L. Chen, G.-F. Chen, C.-C. Chen and Y.-C. Wu, *J. Am. Chem. Soc.*, 2002, **124**, 3508-3509.
19 S. Bhatia, L. C. Camacho and R. Haag, *J. Am. Chem. Soc.*, 2016, **138**, 8654-8666.
20 T. K. Haxton, R. N. Zuckermann and S. Whitelam, *Journal of Chemical Theory and Computation*, 2016, **12**, 345-352.
21 E. J. Robertson, E. M. Nehls and R. N. Zuckermann, *Langmuir*, 2016, **32**, 12146-12158.
22 E. J. Robertson, C. Proulx, J. K. Su, R. L. Garcia, S. Yoo, E. M. Nehls, M. D. Connolly, L. Taravati and R. N. Zuckermann, *Langmuir*, 2016, **32**, 11946-11957.
23 B. Sanii, T. K. Haxton, G. K. Olivier, A. Cho, B. Barton, C. Proulx, S. Whitelam and R. N. Zuckermann, *ACS Nano*, 2014, **8**, 11674-11684.
24 B. Sanii, R. Kudirka, A. Cho, N. Venkateswaran, G. K. Olivier, A. M. Olson, H. Tran, R. M. Harada, L. Tan and R. N. Zuckermann, *J. Am. Chem. Soc.*, 2011, **133**, 20808-20815.
25 R. V. Mannige, T. K. Haxton, C. Proulx, E. J. Robertson, A. Battigelli, G. L. Butterfoss, R. N. Zuckermann and S. Whitelam, *Nature*, 2015, **526**, 415-420.
26 K. T. Nam, S. A. Shelby, P. H. Choi, A. B. Marciel, R. Chen, L. Tan, T. K. Chu, R. A. Mesch, B. C. Lee, M. D. Connolly, C. Kisielowski and R. N. Zuckermann, *Nat Mater*, 2010, **9**, 454-460.
27 B. Sanii, R. Kudirka, A. Cho, N. Venkateswaran, G. K. Olivier, A. M. Olson, H. Tran, R. M. Harada, L. Tan and R. N. Zuckermann, *J Am Chem Soc*, 2011, **133**, 20808-20815.
28 V. M. Kaganer, H. Möhwald and P. Dutta, *Reviews of Modern Physics*, 1999, **71**, 779-819.
29 A.-C. Schöne, T. Roch, B. Schulz and A. Lendlein, *J. Royal Soc. Interf.*, 2017, **14**.
30 A. Chmyrov, T. Sanden and J. Widengren, *J. Phys. Chem. B*, 2010, **114**, 11282-11291.
31 S. B. Ruvinov, X. J. Yang, K. D. Parris, U. Banik, S. A. Ahmed, E. W. Miles and D. L. Sackett, *J. Biol. Chem.*, 1995, **270**, 6357-6369.
32 E. J. Robertson, G. K. Oliver, M. Qian, C. Proulx, R. N. Zuckermann and G. L. Richmond, *Proc. Natl. Acad. Sci. U S A*, 2014, **111**, 13284-13289.
33 R. V. Mannige, T. K. Haxton, C. Proulx, E. J. Robertson, A. Battigelli, G. L. Butterfoss, R. N. Zuckermann and S. Whitelam, *Nature*, 2015, **526**, 415.
34 A. G. Byrne, M. M. Byrne, G. Coker Iii, K. B. Gemmill, C. Spillmann, I. Medintz, S. L. Sloan and B. Wieb van der Meer, in *FRET – Förster Resonance Energy Transfer*, Wiley-VCH Verlag GmbH & Co. KGaA, 2013, Ch. 14, pp. 655-755.
35 L. Albertazzi, F. J. Martinez-Veracoechea, C. M. Leenders, I. K. Voets, D. Frenkel and E. W. Meijer, *Proc. Natl. Acad. Sci. U S A*, 2013, **110**, 12203-12208.
36 F. J. Martinez-Veracoechea and D. Frenkel, *Proc. Natl. Acad. Sci. U S A*, 2011, **108**, 10963-10968.
37 Y. Zhang, H. Zhang, J. Hollins, M. E. Webb and D. Zhou, *Phys. Chem. Chem. Phys.*, 2011, **13**, 19427-19436.
38 P. M. St Hilaire, M. K. Boyd and E. J. Toone, *Biochem.*, 1994, **33**, 14452-14463.
39 S. Bhatia, L. C. Camacho and R. Haag, *J. Am. Chem. Soc.*, 2016, **138**, 8654-8666.
40 G. E. Soto and S. J. Hultgren, *J. Bacteriol.*, 1999, **181**, 1059-1071.
41 S. L. Harris, P. A. Spears, E. A. Havell, T. S. Hamrick, J. R. Horton and P. E. Orndorff, *J. Bacteriol.*, 2001, **183**, 4099-4102.
42 G. Yu, Y. Ma, C. Han, Y. Yao, G. Tang, Z. Mao, C. Gao and F. Huang, *J. Am. Chem. Soc.*, 2013, **135**, 10310-10313.
43 D.-W. Lee, T. Kim, I.-S. Park, Z. Huang and M. Lee, *J. Am. Chem. Soc.*, 2012, **134**, 14722-14725.
44 Y.-b. Lim, S. Park, E. Lee, H. Jeong, J.-H. Ryu, M. S. Lee and M. Lee, *Biomacromol.*, 2007, **8**, 1404-1408.
45 Z. Qi, P. Bharate, C.-H. Lai, B. Ziem, C. Böttcher, A. Schulz, F. Beckert, B. Hatting, R. Mülhaupt, P. H. Seeberger and R. Haag, *Nano Lett.*, 2015, **15**, 6051-6057.

display
ligand

linker

lipid
anchor

+

Nanosheet-forming peptoid

Co-assembly

Multivalent ligand display on peptoid nanosheets

293x190mm (225 x 225 DPI)